

Cite this: *Catal. Sci. Technol.*, 2019,
9, 702

Effect of ammonia on cobalt Fischer–Tropsch synthesis catalysts: a surface science approach

Ali Can Kizilkaya, *^{ab} J. W. Niemantsverdriet ^c and C. J. Weststrate ^c

Ammonia adsorption and decomposition on defect-rich hcp-Co(0001) surfaces were investigated under ultra-high vacuum conditions in order to provide a fundamental explanation for industrially observed ammonia poisoning of cobalt based Fischer–Tropsch synthesis (FTS) catalysts. Temperature-programmed desorption, infrared spectroscopy and work function measurements indicate that undercoordinated sites bind ammonia stronger than sites on flat Co(0001), and they also induce its dehydrogenation. Density functional theory calculations were employed to explore the reactivity of defective Co surfaces using the fcc-Co(211) as a model. The results indicate that the decomposition products (NH_x) adsorb strongly on or around the step site on fcc-Co(211). We find that $\text{NH} (+2\text{H}_{\text{ad}})$, adsorbed in the threefold site on the upper terrace, is equally stable as $\text{NH}_2 (+\text{H}_{\text{ad}})$, adsorbed in the bridge position at the step edge, both being significantly more stable than the equivalent species adsorbed on the flat Co(0001). The calculated activation barriers for $\text{NH}_{3,\text{ad}}$ dehydrogenation steps are in reasonable agreement with the barriers obtained by fitting experimental data. Based on these fundamental insights, poisoning of cobalt nanoparticles during FTS by NH_3 contaminants can be linked mainly to the blocking of undercoordinated sites by strongly adsorbed NH_2 species.

Received 17th August 2018,
Accepted 3rd January 2019

DOI: 10.1039/c8cy01723a

rsc.li/catalysis

1. Introduction

During Fischer–Tropsch synthesis (FTS), a mixture of CO and H_2 (synthesis gas) is converted to hydrocarbon products with a distribution of chain lengths. Co-Based catalysts are primarily used to produce long chain hydrocarbons, along with a small quantity of oxygenates.^{1,2} FTS has regained interest in the last decades mainly due to increase in oil prices and availability of large amounts of natural gas, backed up with environmental and political reasons.³

FTS is applied industrially at a global scale, to convert synthesis gas obtained from coal (e.g. CTL (coal-to-liquids) in South Africa and P.R. China) or natural gas (GTL (gas-to-liquids) in Qatar). Essentially, synthesis gas can be obtained from any carbon containing feedstock, e.g. biomass and even CO_2 and H_2 can be used in its production. Among the metals that are catalytically active for FTS, only cobalt and iron-based catalysts have found commercial use. For the low-temperature (200–250 °C) FTS, cobalt based catalysts are usually preferred. These catalysts exhibit higher stability (i.e.,

slower deactivation) and selectivity to long chain (C_{20+}), linear paraffins (waxes) and lower CO_2 production compared to their iron counterparts, while being relatively more expensive (~250 times) and more susceptible to poisons.⁴ For medium and high temperature applications, iron catalysts are preferred.⁵

Biomass-derived synthesis gas frequently contains a number of contaminants such as NH_3 , HCN, H_2S , carbonyl sulphide (COS), and HCl, which can adversely affect the performance of cobalt catalysts.⁶ Major pathways for the deactivation of cobalt FTS catalysts have been proposed as carbon deposition, sintering and poisoning due to sulphur based compounds, HCN and NH_3 .⁷ Nitrogen-containing compounds are known to be responsible for deactivation of cobalt catalysts.⁸ Patents indicate rapid activity loss due to addition of even ppb levels of ammonia, which can be reversed by mild hydrogen treatment.^{9,10} A number of reports related to the poisoning of FTS catalysts by ammonia and techniques to remove ammonia from the synthesis gas can also be found in the patent literature.^{9–11}

The effect of ammonia on the activity and selectivity of cobalt FTS catalysts has gained interest in recent years due to the potential applications of FTS using synthesis gas derived from biomass.^{6,12–15} Borg *et al.*⁶ concluded that addition of 4.2 ppmv of ammonia did not affect the activity and selectivity of Co/Re/Ni–aluminate catalysts, while other studies confirmed the deactivation of supported cobalt FTS catalysts due

^a Department of Chemical Engineering, Izmir Institute of Technology, 35430, Izmir, Turkey. E-mail: alicankizilkaya@iyte.edu.tr

^b Laboratory for Physical Chemistry of Surfaces, Eindhoven University of Technology, 5600 MB, Eindhoven, The Netherlands

^c Syncat@DIFFER, Syngaschem BV, De Zaale 20, 5612 AJ, Eindhoven, The Netherlands

to 10–2500 ppmv or 1–1200 ppmw ammonia addition, together with a decrease in methane and an increase in C_{5+} selectivity.^{12–15}

In particular, Pendyala *et al.* have investigated the effect of NH_3 on Pt-promoted cobalt/alumina FTS catalysts in a continuously stirred tank reactor (CSTR) at 493 K and 1.9 MPa. They concluded that ammonia addition resulted in irreversible deactivation (~5%) of the catalyst, accompanied by ~1.5% decrease in CH_4 selectivity and ~2% increase in C_{5+} selectivity, for the range of 1–1200 ppmw of ammonia addition.¹² In a later study,¹³ Pendyala *et al.* confirmed their findings for both alumina and titania supported cobalt FTS catalysts. Instead, for silica supported catalysts, ammonia was reported to increase the selectivity to C_1 – C_4 products, while decreasing the selectivity to C_{5+} . Pendyala *et al.* also investigated the effect of ammonia addition on the selectivities of various products for Pt-promoted cobalt/alumina catalysts.¹⁴ They concluded that the addition of ammonia increased the selectivity to olefins and decreased the selectivity to alcohols. The possible reasons behind these effects were proposed as competitive adsorption of NH_3 with CO and H_2 ,¹² inhibition of chain growth termination by ammonia¹⁴ or the formation of an inactive cobalt nitride phase.¹⁴ Ordonsky *et al.* also investigated the effect of NH_3 on supported Fe and Co-based FTS catalysts. Their findings confirm that ammonia addition decreases selectivity for CH_4 and increases the C_{5+} selectivity for Co-based catalysts, together with their irreversible deactivation.¹⁵ The origins of the phenomena were proposed as the decrease in the hydrogenation activity of the catalysts, due to formation of cobalt nitride on step edges of cobalt nanoparticles. From a more fundamental perspective, Ma *et al.* investigated NH_3 decomposition on clean and O-covered Co(111), Co(100) and Co(110) surfaces by density functional theory calculations.¹⁶ They pointed out that the decomposition of NH is the rate limiting step and N or NH species are likely responsible for the deactivation of Co-based catalysts in the presence of oxygen. Nevertheless, the origins of the observed phenomena, *i.e.* why ammonia acts as a poison for cobalt FTS catalysts and how it influences the selectivity, remains unclear.

Due to the complexity of the FTS reaction, where various factors contribute to the observed activity and selectivity, a simplified model of the catalyst is beneficial to obtain detailed understanding at a more fundamental (*i.e.*, the molecular) level. The active state of cobalt FTS catalysts is widely accepted as cobalt nanoparticles in metallic state.³ Predictions of face centered cubic (fcc) cobalt particle shapes in literature^{17,18} show that the surface of the nanoparticle predominantly exposes flat (111) and (100) terraces, whereas the concentration of monoatomic step edge sites is in the order of 10%. Earlier we reported on how NH_x effects CO and H_2 adsorption on a flat Co(0001) surface,¹⁹ giving information about the reactivity of the flat terraces present on the cobalt nanoparticle. Our results indicated that ammonia desorption is kinetically favored over NH_3 decomposition on flat cobalt surfaces. NH_3 selectively inhibits the dissociative adsorption

of H_2 on flat terraces, while not affecting the adsorption capacity of CO. We concluded that NH_x species are most likely responsible for the deactivation of cobalt FTS catalysts, due to their high stabilities.

In the present study, we investigate how ammonia interacts with undercoordinated (defect) sites. The decomposition of NH_3 on defective Co(0001) is investigated experimentally using a combination of temperature programmed decomposition, infrared spectroscopy and work function measurements, to observe the role of defects in NH_3 decomposition on cobalt surfaces and to obtain activation barriers of the NH_x dehydrogenation steps ($x = 1, 2, 3$). Density functional theory (DFT) modelling is also used to calculate adsorption energies and decomposition barriers for NH_x on the stepped Co(211) surface to compare with experimental results. The findings indicate that the deactivation of Co-based FTS catalysts due to ammonia can be attributed to the blocking of undercoordinated sites by strongly bound NH_2 .

2. Experimental section

Two Co(0001) single crystals were used in the two different vacuum systems described hereafter. In both systems the sample was clamped between tungsten wires, which were used for heating and cooling the sample. The sample temperature was measured using a chromel–alumel thermocouple spot welded to the back of the crystal. The single crystal surfaces were cleaned by 20 minute long cycles of argon ion sputtering ($E = 1.0$ keV) while the sample was held at 630 K, followed by annealing at 630 K in vacuum for another 20 minutes. LEED measurements confirmed that the surface ordering was restored after cleaning. Sample cleanliness was routinely tested by CO temperature programmed desorption (TPD), which proved to be sensitive to the presence of carbon and oxygen contaminations.^{20,21} The role of defect sites was investigated by intentionally introducing defect structures on the flat Co(0001) surface. This sputter-damaged surface [referred to as the “defective” Co(0001) surface] was generated by sputtering the surface with 1 kV Ar^+ ions for 5 minutes while the sample was held at 320 K. All gases were dosed by backfilling the chamber and no further purification steps were used. Exposures are reported in Langmuir (L, 1×10^{-6} Torr s), calculated using uncorrected ion gauge readings.

Temperature programmed desorption (TPD) and work function (TP-WF) measurements were performed in a UHV system with a base pressure of $\sim 4 \times 10^{-10}$ mbar. The system is equipped with LEED/Auger optics, a Kelvin probe equipped with a stainless steel tip, and a sputter gun for sample cleaning. The quadrupole mass spectrometer is placed inside a separately pumped compartment which is connected to the main UHV chamber by a 5 mm circular hole. By placing the sample surface of our 8 mm disc-shaped sample in close proximity (~ 1 mm) to the aperture, desorption signals from other parts of the sample holder could be eliminated.

The vacuum system used for infrared (IR) and additional TPD studies consists of two chambers, as outlined in more

detail previously.²² The top chamber ($\sim 2 \times 10^{-10}$ mbar) is equipped with a mass spectrometer, LEED optics, an X-ray source and electron energy analyzer, a sputter gun for sample cleaning and a Kelvin probe. The lower chamber ($< 1 \times 10^{-10}$ mbar) contains facilities for reflection absorption infrared spectroscopy (RAIRS), where the infrared beam is specularly reflected from the front face of the single crystal. IR measurements were performed with a resolution of 4 cm^{-1} using a Nicolet iS10 spectrometer. The spectra reported were obtained after subtracting a background spectrum from the measured data and by averaging over 256 scans.

3. Computational methods

Periodic density functional calculations were performed using the Vienna *ab initio* simulation package (VASP).^{23,24} Plane-waves with a kinetic energy up to 400 eV were included. The exchange–correlation energy was calculated within the generalized gradient approximation (GGA) using Perdew–Wang 91 (ref. 25) functional and ultrasoft Vanderbilt²⁶ type pseudopotentials (US-PP) as supplied by Kresse and Hafner.²⁷ The choice of using US-PP is based on the previous successful applications of US-PP for simulating cobalt single crystal surfaces^{28,29} and the match of our DFT generated results with the experimental data.

It is known that the long range dispersion (van der Waals) interactions can play a role in the physisorption of molecules on metal surfaces. However, for chemisorbed species the DFT functionals that incorporate these interactions are known to overestimate the adsorption energy.³⁰ Therefore, in our investigation of NH_3 adsorption (chemisorption) on the Co(211) surface, van der Waals interactions were not taken into account.

The reciprocal space was sampled with a $(9 \times 9 \times 1)$ *k*-points grid automatically generated using Monkhorst–Pack method.³¹ Fractional occupancies were calculated using a first-order Methfessel–Paxton smearing function³² with a width of 0.2 eV and an energy convergence smaller than 10^{-4} eV was used.

The fcc-Co(211) surface was modelled with 4 layers of metal atoms. A vacuum height of at least 10 \AA was inserted between slabs to avoid coupling between successive slabs in the *z*-direction. The calculations were performed in $p(2 \times 2)$ unit cells, to simulate an NH_3 coverage of 0.25 ML. The 0.25 ML coverage is selected since that is the saturation coverage of NH_3 on the flat Co(0001) surface,¹⁸ and our previous findings indicate that coadsorbed CO and H_2 do not inhibit the adsorption of NH_x on the surface. The relative positions of the cobalt atoms of the bottom two layers were kept frozen at the computed bulk positions, while the upper two layers were free to relax. The dipole moment due to the usage of an asymmetric slab was removed with standard dipole correction.

Equilibrium was reached when the forces on the atoms of the top two metal layers and the atoms placed on top of the metal slab were less than 0.01 eV \AA^{-1} in each of the Cartesian

directions. All reported energies are zero-point energy (ZPE) corrected. Saddle points in the minimum energy path were found with the nudged elastic band (NEB) method.³³ NEB calculations were continued until the image with the highest energy in the minimum energy path converged in energy with 10^{-4} eV tolerance. The likely transition state (TS) structures produced by the NEB method were further refined until the forces on atoms were less than 0.01 eV \AA^{-1} . All TS structures were characterized by vibrational frequency analysis within the harmonic oscillator approximation as having a single mode of imaginary frequency. During the vibrational analysis, the relaxed atoms were displaced from their equilibrium positions twice (0.02 \AA). For the NEB and vibrational frequency analyses, all atoms of the metal slab were kept fixed while the adsorbates were fully relaxed.

All the parameters (number of layers, energy cut-off, *k*-points, *etc.*) were fully optimized (the smaller sets which reproduced the same results within 0.1 eV were chosen). The DFT computed energies are expressed in kJ mol^{-1} throughout the article to better compare the theoretical findings with the experimental data.

The adsorption energies of NH_x and H were calculated with respect to gas phase NH_3 and H_2 respectively, according to following equations [in order to stoichiometrically balance the dehydrogenated products (NH_x) with respect to gas phase NH_3 , the energy of H atom adsorbed on a separate slab, was added to the system]:

$$E_{\text{ad}}^{\text{NH}_x} = E_{\text{NH}_x, \text{ad}} + (3-x)E_{\text{H,ad}} - (4-x)E_{\text{slab}} - E_{\text{NH}_3, \text{g}}$$

$$E_{\text{ad}}^{\text{H}} = E_{\text{H,ad}} - E_{\text{slab}} - 0.5E_{\text{H}_2, \text{g}}$$

where E_{ad}^{X} indicates the adsorption energy of X, $E_{\text{X,ad}}$ indicates the total energy of the system where X is adsorbed on Co(211), E_{slab} indicates the energy of the clean Co(211) (no adsorbates) and $E_{\text{x,g}}$ indicates the energy of molecule X in gas phase. All adsorption sites on Co(211) were tested for all species.

4. Results

4.1. Molecular modelling of NH_3 decomposition on the stepped Co(211) surface by DFT calculations

The stepped Co(211) surface is chosen as a model surface, as it exposes monoatomic steps, the most abundant type of defect sites exposed by a cobalt nanoparticle.¹⁷ More specifically, it exposes the so-called B5 site, which is thought to be particularly active for direct CO dissociation.^{34,35} In order to investigate the role of defect (undercoordinated) sites (steps, kinks, edges, *etc.*), the energetics of the ammonia decomposition pathway on the stepped Co(211) surface were calculated.

The relative energies of NH_3 and its decomposition products (NH_x) are calculated for different adsorption sites on Co(211). Fig. 1 shows the structure of the Co(211) surface used for the calculations and the different adsorption sites that were considered.

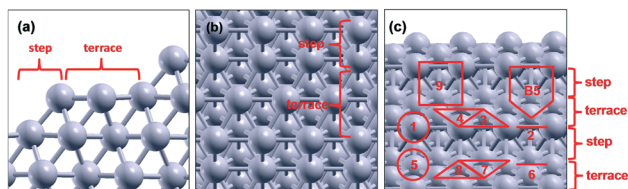


Fig. 1 Views of the Co(211) surface. (a) Side view, (b) top view and (c) front view that shows the particular arrangement of atoms which is called the “B5 site” and the adsorption sites: 1) top (step edge), 2) bridge (step edge), 3) fcc (step edge), 4) hcp (step edge), 5) top (terrace), 6) bridge (terrace), 7) fcc (terrace), 8) hcp (terrace), 9) step.

Table 1 lists the most stable adsorption sites, adsorption energies, relative stabilities of NH_x and H species and activation barriers of decomposition for NH_x on Co(211), while Fig. 2 depicts the relative energies of the various stages of $\text{NH}_{3,\text{ad}}$ dehydrogenation on this surface. In particular, the energy values following the adsorption sites indicate the difference in adsorption energy with respect to the most stable adsorption sites. *E.g.*, a value of zero indicates that this adsorption site is the most stable. A positive value indicates how much the adsorption of the molecule is destabilized on the particular site with respect to the most stable site, calculated by subtracting the adsorption energy on that particular site from the most stable adsorption site. For some calculations, no convergence could be obtained for the indicated adsorption site (the species desorbed to the gas phase or diffused to another adsorption site). These results are indicated in Table 1 by “—”.

Table 1 shows that the preferred adsorption sites for all species are located on or around the step site. In particular, the results indicate that NH_x are considerably more stable on the step site compared to on terrace sites.

Fig. 2 shows that activation barrier for ammonia decomposition on Co(211) (72 kJ mol^{-1}) is lower than the adsorption energy of ammonia (81 kJ mol^{-1}). This means that ammonia decomposition is favored over desorption on Co(211) unlike on Co(0001), for which our previous study showed that the ammonia decomposition barrier (105 kJ mol^{-1}) is significantly higher than the ammonia adsorption energy (59 kJ mol^{-1} for $\theta_{\text{NH}_3} = 0.06 \text{ ML}$).¹⁹

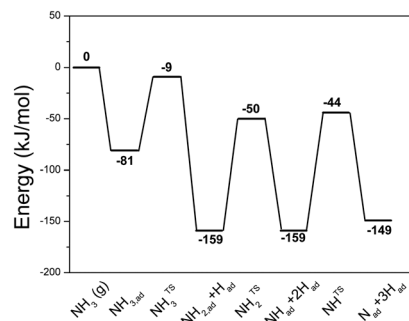


Fig. 2 Potential energy diagram (PED) for 0.25 ML $\text{NH}_{3,\text{ad}}$ decomposition sequence on Co(211). X_{ad} represents adsorbed species. All reported energies correspond to the most stable adsorption site. Zero-point energy corrections are included in the data.

4.2. The role of undercoordinated sites in ammonia decomposition: experimental observations

4.2.1. Ammonia adsorption on the sputter-damaged (defective) Co(0001) surface.

The adsorption of ammonia on defect sites on Co(0001) surface was investigated experimentally using a combination of RAIRS, TPD and TP-WF.

A series of IR spectra recorded during dosing of NH_3 to the defective Co(0001) surface is shown in Fig. 3(a), together with spectra for the same dose obtained on the flat surface (intensity for flat surface spectra divided by 4 to facilitate comparison). The temperature during this experiment was kept at 140 K to minimize the build-up of multilayers of NH_3 , which are known to desorb around this temperature.³⁶ The only discernible vibration in the IR absorption spectra is the symmetric N–H bending mode of $\text{NH}_{3,\text{ad}}$ between $1180\text{--}1100 \text{ cm}^{-1}$. For low doses this absorption band is located around 1160 cm^{-1} on the defective (sputter-damaged) surface. The peak position initially shifts slightly when the dose is increased until about 0.7 L, with the frequency being significantly higher than that found after an equivalent dose on the flat surface. For doses $>0.7 \text{ L}$ a new component develops at 1120 cm^{-1} . This frequency is close to the value reported for ammonia ice layers.³⁷ We therefore attribute this band to the ammonia molecules forming a second physisorbed ammonia layer. The IR signal intensity, plotted in Fig. 3(b), shows a

Table 1 Adsorption sites, adsorption energies, activation barriers of decomposition, reaction enthalpies and relative stabilities (with respect to the most stable site) of NH_x and H species on Co(211)

Adsorbate	NH_3	NH_2	NH	N	H
E_{ad} (kJ mol^{-1})/site	–81/top (step edge)	–159/bridge (step edge)	–159/hcp (step edge)	–149/step	–41/hcp (step edge)
E_{act} (kJ mol^{-1}) (decomposition)	72	109	115	n.a	n.a
ΔH (kJ mol^{-1})	–32	–53	12	n.a	n.a
Top (step edge)	0	102	—	278	—
Bridge (step edge)	—	0	—	—	3
fcc (step edge)	—	95	38	52	8
hcp (step edge)	—	83	0	0.3	0
Top (terrace)	—	—	—	—	—
Bridge (terrace)	—	—	—	—	—
fcc (terrace)	—	132	—	40	19
hcp (terrace)	—	114	40	40	12
Step	—	76	8	0	22

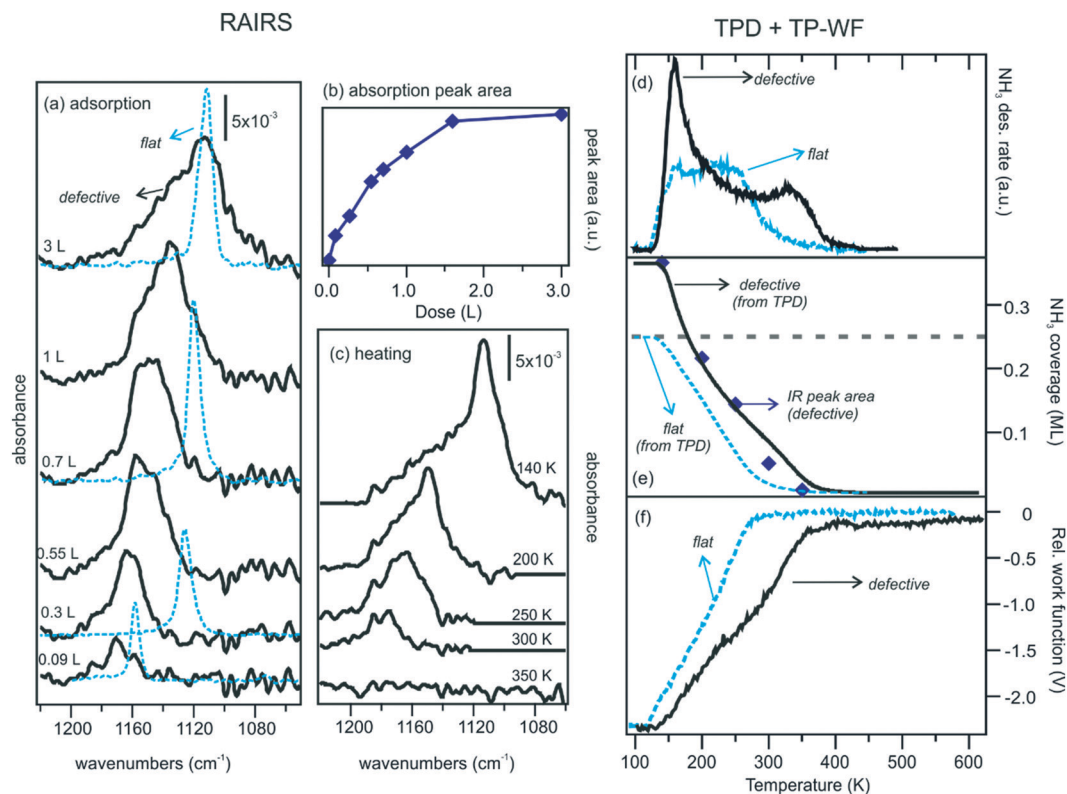


Fig. 3 (a) IR absorption spectrum during NH_3 uptake at 140 K on the defective Co(0001) surface. Dashed line shows data for the flat surface as reference (signal strength divided by 4 to facilitate comparison). (b) IR peak area as a function of NH_3 dose. (c) IR spectra after heating to the indicated temperatures. (d) $m/z = 17$ desorption traces for the $\text{NH}_{3,\text{ad}}$ -saturated surface at 100 K, both for the sputtered and flat surface. (e) IR peak area (\blacklozenge) during heating together with the peak areas from TPD. The dashed grey line marks the coverage at which the first chemisorbed layer is saturated. (f) Work function measurements during heating. A heating rate of 1 K s^{-1} was used for all temperature programmed experiments.

steadily increase as a function of NH_3 dose until saturation is reached after a dose of $\sim 1.6 \text{ L}$.

The band around 1120 cm^{-1} disappears when the sample is heated to 200 K, whereas the band around 1160 cm^{-1} is still visible after heating to 300 K [Fig. 3(c)]. Fig. 3(d) shows the thermal desorption spectra after dosing NH_3 at 100 K, for both the flat and the defective surfaces. After introducing defects by sputter damaging the surface, we find an additional, high temperature NH_3 peak that was absent for the flat surface. This indicates that NH_3 adsorbs more strongly on defect sites compared to on terrace sites. By integration of the TPD spectra the change of θ_{NH_3} as a function of temperature can be obtained. These data are plotted in Fig. 3(e) alongside the IR peak intensity derived from the data shown in Fig. 3(c). We find a reasonable match between the change of the IR peak height and the ammonia coverage as derived from the TPD data, indicating that the disappearance of the symmetric N–H stretch of ammonia can be attributed to ammonia desorption.

Ammonia readily forms multilayers, making it experimentally difficult to selectively populate only to the first chemisorbed layer during ammonia adsorption. In Fig. 3(d) the ammonia desorption peak at 150 K for the defective Co(0001) surface can be attributed in part to desorption from a second, physisorbed NH_3 layer. The contribution of this second layer explains why the total area of the TPD spectrum is higher for

the defective surface, thus interfering with accurate determination of the saturation coverage for chemisorbed $\text{NH}_{3,\text{ad}}$ on both flat and defective Co(0001) surfaces.

Our earlier experiments related to NH_3 adsorption on Co(0001)¹⁹ and previous studies on other metals^{36,38} indicate that the work function of the sample only responds to chemisorbed $\text{NH}_{3,\text{ad}}$, whereas it is insensitive to the physisorbed multilayers of ammonia. Fig. 3(f) shows TP–WF measurements after dosing $\text{NH}_{3,\text{ad}}$ on both the flat and the defective surface. It should be noted that surface roughening by sputtering causes a decrease of the work function by about 400 meV compared to the clean, flat surface. During heating in vacuum after the sputtering treatment, the work function increases between 300–400 K and the clean surface value is restored after that. This contribution was eliminated from the data shown in Fig. 3(e) by subtracting the work function change measured while heating the defective surface in vacuum from the data obtained during heating of the NH_3 -covered surface.

The work function data show that the work function changes by -2.3 V after saturating the surface with $\text{NH}_{3,\text{ad}}$, for both the flat and the defective surface. This means that adsorption capacity of the surface for NH_3 , which we determined to be around 0.25 ML in our previous experiments, is not affected significantly by the sputtering treatment. During heating the change of work function matches very well with

change of surface coverage as deduced from the TPD data. For both the flat and the defective surface two desorption peaks can be discerned. On the flat surface 50% of the chemisorbed $\text{NH}_{3,\text{ad}}$ desorbs around 160 K, whereas for the defective surface this low temperature desorption peak is found at 190 K. The influence of defect sites is even more pronounced for the high temperature $\text{NH}_{3,\text{ad}}$ desorption peak, which shifts from 250 K for the flat surface to around 330 K for the defective surface. These data thus clearly show that molecular ammonia adsorption is stronger on defect sites compared to flat terrace sites.

4.2.2. Ammonia decomposition on defect sites. Proof for defect-induced ammonia decomposition on the defective surface is evident from the production of hydrogen in the TPD experiment. The procedure to create defects, *via* sputtering at 320 K, inevitably leads to a significant quantity of H_{ad} produced by H_2 adsorption from the residual gas.²⁹ ND_3 was therefore used in addition to NH_3 to for a quantitative evaluation of the stepwise $\text{ND}_{3,\text{ad}}$ decomposition process.

Fig. 4(a) shows the desorption traces of H_2 , HD, and D_2 during heating of the $\text{ND}_{3,\text{ad}}$ -covered defective surface. Quantitative analysis of the peak area shows that the total amount of D produced (both as HD and D_2) is ~ 0.15 ML, *i.e.* around 0.05 ML $\text{ND}_{3,\text{ad}}$ was decomposed on the surface. In addition to this, around 0.22 ML H_{ad} was adsorbed from the residual

gas alongside the $\text{ND}_{3,\text{ad}}$. The vast majority of deuterium desorbs above 360 K (both as HD and as D_2), above the temperature where H_{ad} is known to desorb (as H_2) from Co(0001). This implies that the N–D bonds remain intact up to around 360 K. The HD and D_2 desorption peaks therefore directly reflect the rate of $\text{ND}_{x,\text{ad}}$ decomposition, since the D_{ad} produced instantly leaves the surface and is detected (as D_2 or HD) by the mass spectrometer. The minor quantity of HD desorbs alongside H_2 is tentatively attributed to isotopic exchange between surface H_{ad} and ND_3 [labelled as ‘isotopic exchange’ in Fig. 4(b)].

The desorption trace of D, derived from the D_2 signal and 50% of the HD signal [shown in Fig. 4(b)], was used to extract the barriers for each $\text{ND}_{x,\text{ad}}$ decomposition step. In our previous study on the flat Co(0001) surface,¹⁹ electron-induced dissociation of $\text{NH}_{3,\text{ad}}$ was found to produce NH_{ad} at a low surface temperature. The H_2 desorption spectrum recorded afterwards, shown in Fig. 4(c), reveals that 2/3 of the hydrogen desorbs around 350 K, whereas the remaining 1/3 desorbs around 440 K. The 350 K peak was attributed to desorption of the 2 H_{ad} produced per $\text{NH}_{3,\text{ad}}$ dissociated to NH_{ad} during exposure to the electron beam. The 440 K peak is attributed to decomposition of NH_{ad} . It can be fitted using a Gaussian peak shape, as shown in Fig. 4(c). Using the Red-head equation for first order reactions and a pre-factor of $1 \times$

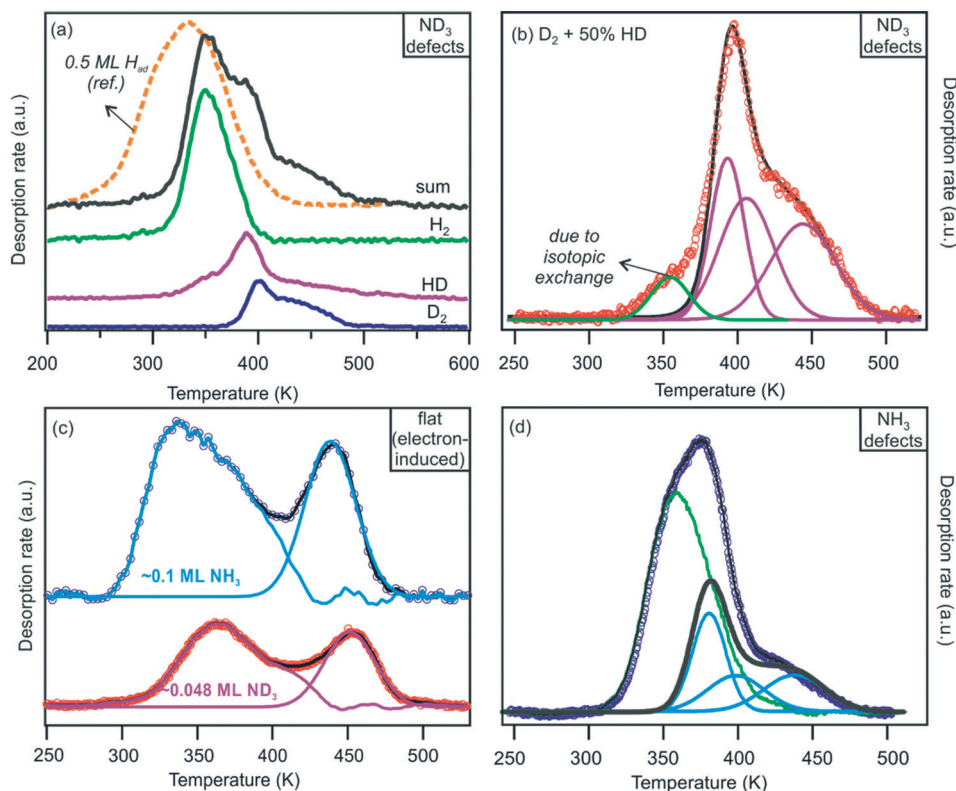


Fig. 4 Hydrogen desorption during ammonia decomposition on defective Co(0001). (a) Desorption traces for $m/z = 2$ (H_2), $m/z = 3$ (HD) and $m/z = 4$ (D_2) during heating of an ND_3 -covered surface. (b) Deconvolution of the sum of all deuterium-containing desorption peaks. (c) H_2 (D_2) desorption after electron-induced NH_3 (ND_3) dissociation on flat Co(0001) surface, adapted from (ref. 19) and used to evaluate results on defective surface. (d) Deconvolution of the H_2 desorption spectrum after NH_3 decomposition on defective Co(0001). A heating rate of 1 K s^{-1} was used for all experiments.

10^{13} an activation energy of 119 kJ mol^{-1} was found. The D_2 desorption peak due to ND decomposition (produced by electron-induced ND_3 dissociation) is found at about 10 degrees higher temperature, which translates to a barrier of $\sim 123 \text{ kJ mol}^{-1}$ in our analysis.

The insights about NH_{ad} (ND_{ad}) decomposition obtained from the electron-induced $\text{NH}_3/(\text{ND}_3)$ dissociation experiment were used to deconvolute the deuterium desorption trace due to ND_3 decomposition on the sputter-damaged surface, as shown in Fig. 4(b). We find that the D_2 desorption at the high temperature end of the spectrum on the defective surface can be accounted for by using the shape and position derived from ND_{ad} decomposition after electron beam exposure. From there, two additional peaks with the same peak area as the peak attributed to ND_{ad} were added to account for $\text{ND}_{2,\text{ad}}$ and $\text{ND}_{3,\text{ad}}$ dehydrogenation, respectively.

The resulting peak positions were then used to fit the data for NH_3 decomposition on the defective surface, shown in Fig. 4(d). In this analysis, the peak positions needed to be shifted to lower as a result of kinetic isotope effects. In this way, it was possible to obtain a satisfactory fit of this data as well, despite the presence of 0.22 ML additional hydrogen that adsorbed from the residual gas. In the fitting result the three peaks attributed to $\text{NH}_{x,\text{ad}}$ decomposition steps have approximately equal peak areas for the three peaks, and furthermore, the desorption peak attributed to the hydrogen adsorbed from the residual gas occurs at similar temperature as found for hydrogen desorption from an H_{ad} -covered surface. The activation barriers obtained as a result of this fitting procedure and their comparison to DFT generated results are shown in Table 2.

Table 2 indicates that there is a good match (max. error $< 7 \text{ kJ mol}^{-1}$) between experimental/DFT generated results, with the exception of NH_3 decomposition on the sputter-damaged surface, for which the experimentally determined barrier is 30 kJ mol^{-1} higher than the computed barrier. The kinetic isotope effect (KIE) is evident from the results, in all cases a typical KIE effect of $2\text{--}5 \text{ kJ mol}^{-1}$ is observed.

5. Discussion

Fig. 5 represents a comparison of the adsorption energies of $\text{NH}_{x,\text{ad}}$ species in their most stable site on the $\text{Co}(211)$ surface with the values computed earlier for the flat $\text{Co}(0001)$

Table 2 Comparison of experimental and DFT calculated activation barriers for $\text{NH}_{x,\text{ad}}$ decomposition reactions

Reaction	Defective $\text{Co}(0001)/\text{Co}(211)$ (experimental/DFT ^a)
$\text{NH} \rightarrow \text{N} + \text{H}$	117/115
$\text{NH}_2 \rightarrow \text{NH} + \text{H}$	107/109
$\text{ND}_2 \rightarrow \text{ND} + \text{D}$	110/—
$\text{NH}_3 \rightarrow \text{NH}_2 + \text{H}$	102/72
$\text{ND}_3 \rightarrow \text{ND}_2 + \text{D}$	106/—
$\text{NH}_{3,\text{ad}} \rightarrow \text{NH}_3(\text{g})$	88/81

^a Experimental data obtained on defective $\text{Co}(0001)$ surfaces are compared with DFT results on $\text{Co}(211)$.

surface.¹⁹ It is clear that all $\text{NH}_{x,\text{ad}}$ species, including $\text{NH}_{3,\text{ad}}$, adsorb much stronger on or close to the undercoordinated atoms exposed at the step edge than on the flat surface. This diagram furthermore shows a higher propensity towards ammonia decomposition on the stepped surface compared to that on the flat surface. With the barrier of decomposition being lower than the desorption barrier of dissociation extensive ammonia decomposition can be expected on this specific surface.

The DFT results also shed more light on the origin of the difference in activation barrier for NH_3 decomposition on $\text{Co}(0001)$ vs. $\text{Co}(211)$. The transition and final states of NH_3 decomposition on $\text{Co}(0001)$ and $\text{Co}(211)$ are plotted in Fig. 6.

Fig. 6 shows that the transition states for NH_3 decomposition on $\text{Co}(0001)$ and $\text{Co}(211)$ differ in terms of their transition state geometries. NH_2 and H species share the same surface metal atom on $\text{Co}(0001)$, while they are located on different metal atoms on $\text{Co}(211)$. The strong repulsion due to the sharing of the metal atom would lead to a higher activation barrier on $\text{Co}(0001)$.³⁵ Another factor that affects the activation barrier is the resemblance between the transition and final states on the particular surface. The adsorption sites for H_{ad} and $\text{NH}_{2,\text{ad}}$ in the final state on $\text{Co}(211)$ resemble the transition state more than they do on $\text{Co}(0001)$, where the adsorption states in the final state adsorption geometry is significantly different from the transition state geometry. Both of these factors can play a role for the lower activation barrier for NH_3 on $\text{Co}(211)$ compared to $\text{Co}(0001)$.³⁵

The experimental data qualitatively confirm these findings. The TPD data shows a higher desorption temperature for ammonia on defects, thereby confirming that ammonia adsorbs more strongly on undercoordinated sites. Furthermore, we find that such sites facilitate decomposition of $\text{NH}_{3,\text{ad}}$, a process that occurs around 360 K. The activation barrier derived for this process, 102 kJ mol^{-1} , is significantly higher than the computed value of 72 kJ mol^{-1} . This may in part be attributed to the difference in nature of the defect sites present on the sputtered surface compared to the step site model used in the calculations. Furthermore, the

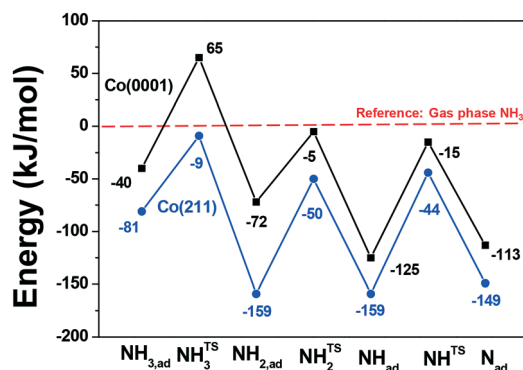


Fig. 5 Comparison of potential energy diagrams for 0.25 ML $\text{NH}_{3,\text{ad}}$ decomposition sequence on $\text{Co}(0001)$ and $\text{Co}(211)$. X_{ad} represents adsorbed species. All reported energies correspond to the most stable adsorption site. Zero-point energy corrections are included in the data.

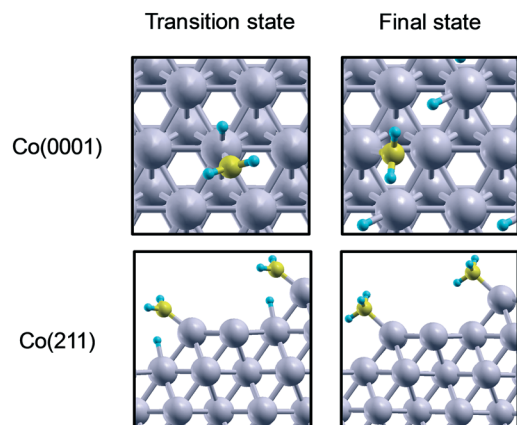


Fig. 6 Transition and final states of ammonia decomposition on Co(0001) and Co(211).

inevitable surface hydrogen present during the experiments may suppress the dissociation reaction. Our proposition is supported by the fact that the difference between computed and observed barriers for $\text{NH}_{2,\text{ad}}$ and NH_{ad} decomposition, which occur after H_2 desorption, are much smaller ($<2 \text{ kJ mol}^{-1}$) than that for the first decomposition step.

We can put these results into the context of Fischer-Tropsch catalysis if we consider the active phase to consist of cobalt nanoparticles which expose both flat terraces as well as monoatomic step sites such as those exposed on the Co(211) surface used in this study. The specific structure exposed at the step on Co(211) is of particular interest in the FTS context since these sites are particularly active for direct dissociation of CO.^{34,35} Step sites are also important for the dissociative adsorption of H_2 to form surface hydrogen. Our results show that ammonia binds particularly strongly on those sites as well. In addition, dissociation occurs on such sites already at relatively low pressures and temperatures, and it produces strongly bound $\text{NH}_{x,\text{ad}}$ species. Although ammonia adsorption and dissociation would also be possible on terrace sites the higher stability of $\text{NH}_{x,\text{ad}}$ at step edge sites means that $\text{NH}_{x,\text{ad}}$ species produced on the terrace would eventually end up at step edge sites as well via surface diffusion. With adsorption energies in the order of $150\text{--}160 \text{ kJ mol}^{-1}$ [relative to $\text{NH}_3(\text{g})$], significantly higher than the adsorption energies of CO and H_2 , $\text{NH}_{x,\text{ad}}$ will accumulate even when the partial pressure of ammonia is low, *i.e.* when NH_3 is present only in ppm levels in the reactant gas. In view of the similar stabilities of NH and NH_2 adsorbed at the step edge, $\text{NH}_{2,\text{ad}}$ is expected to dominate under FTS conditions where surface hydrogen is present on the surface as well.

The notion that ammonia present in ppm levels in the reactant gas eventually leads to build-up of NH_2 adsorbed on the bridge position at a step edge can rationalize the observed influence of ammonia in applied catalysis. By blocking of these active sites for CO dissociation the overall activity of the catalyst is expected to go down. But, since the same sites catalyze dissociative H_2 adsorption, partial poisoning of these sites will also suppress hydrogen adsorption and hydrogenation reac-

tions in FTS, as demonstrated previously.¹⁹ Thus, our findings also support the previous experimental studies stating that NH_3 addition increases the selectivity to C_{5+} hydrocarbons by creating a hydrogen deficient cobalt surface.^{12–14}

Conclusions

Aiming at a molecular level explanation related to NH_3 poisoning of cobalt-based FTS catalysts, NH_3 adsorption and decomposition on defective and sputtered Co(0001) surfaces were investigated under ultra-high vacuum conditions using TPD, WF measurement and IRS. Co(211) surface was used as a computational model for defective surfaces and the experimental data obtained was combined with DFT results. Temperature-programmed experiments indicate that the cobalt surface defects are active in decomposing NH_3 around 360 K already under UHV conditions. DFT calculations confirm these findings as the NH_3 decomposition over monoatomic steps on the Co(211) surface is kinetically favored with an activation barrier of 71 kJ mol^{-1} , compared to an adsorption energy of 82 kJ mol^{-1} . The adsorption energy and decomposition barriers of NH_3 are in reasonable agreement with the barriers obtained by fitting of experimental data. DFT findings also indicate that the decomposition products (NH_x) adsorb strongly on or around the step site on Co(211). Based on these fundamental insights we propose that the industrially observed NH_3 poisoning of cobalt nanoparticles can be attributed prevalently to the blocking of undercoordinated sites that are necessary for CO decomposition by strongly adsorbed NH_2 species.

Conflicts of interest

There are no conflicts of interest to declare.

Acknowledgements

A. C. K. thanks I. M. Ciobica for support related to the computational model for defective sites and Pieter van Helden for valuable comments related to ammonia adsorption on cobalt surfaces. The project was part of the collaboration between Eindhoven University of Technology and Sasol Group Technology. Funding for this project was supplied by the European Graduate School on Sustainable Energy of DTU-TUM-TU/e. Syngaschem BV acknowledges substantial funding from Synfuels China Technology, Co. Ltd.

References

- 1 F. Fischer and H. Tropsch, *Brennst.-Chem.*, 1923, 4, 276–285.
- 2 F. Fischer and H. Tropsch, *Brennst.-Chem.*, 1926, 7, 97–104.
- 3 J. van de Loosdrecht, F. G. Botes, I. M. Ciobica, A. Ferreira, P. Gibson, D. J. Moodley, A. M. Saib, J. L. Visagie, C. J. Weststrate and J. W. Niemantsverdriet, in *Comprehensive Inorganic Chemistry*, Elsevier Ltd., 2nd edn, 2013, vol. 7, pp. 525–557.
- 4 M. E. Dry, *Catal. Today*, 2002, 71, 227–241.

- 5 J. Xu, Y. Yang and Y.-W. Li, *Fuel*, 2015, **152**, 122–130.
- 6 O. Borg, N. Hammer, B. C. Enger, R. Myrstad, O. A. Lindvg, S. Eri, T. H. Skagseth and E. Rytter, *J. Catal.*, 2011, **279**, 163–173.
- 7 A. M. Saib, D. J. Moodley, I. M. Ciobica, M. M. Hauman, B. H. Sigwebela, C. J. Weststrate, J. W. Niemantsverdriet and J. van de Loosdrecht, *Catal. Today*, 2010, **154**, 271–282.
- 8 C. H. Bartholomew, *Appl. Catal., A*, 2001, **212**, 17–60.
- 9 S. C. Leviness, C. J. Mart, W. C. Behrmann, S. J. Hsia and D. R. Neskora, *WIPO Pat.*, 98/50487, 1998.
- 10 J. Inga, P. Kennedy and S. Leviness, *US Pat.*, 2005/0154069A1, 2005.
- 11 R. J. Koveal and S. C. Leviness, *US Pat.*, 6107353, 2000.
- 12 V. R. R. Pendyala, M. K. Gnanamani, G. Jacobs, W. Ma, W. D. Shafer and B. H. Davis, *Appl. Catal., A*, 2013, **468**, 38–43.
- 13 V. R. R. Pendyala, G. Jacobs, C. Bertaux, S. Khalid and B. H. Davis, *J. Catal.*, 2016, **337**, 80–90.
- 14 V. R. Rao Pendyala, W. D. Shafer, G. Jacobs, M. Martinelli, D. E. Sparks and B. H. Davis, *RSC Adv.*, 2017, **7**, 7793–7800.
- 15 V. V. Ordonsky, A. Carvalho, B. Legras, S. Paul, M. Virginie, V. L. Sushkevich and A. Y. Khodakov, *Catal. Today*, 2016, **275**, 84–93.
- 16 F. F. Ma, S. H. Ma, Z. Y. Jiao and X. Q. Dai, *Appl. Surf. Sci.*, 2017, **405**, 71–78.
- 17 P. van Helden, I. M. Ciobica and R. L. J. Coetzer, *Catal. Today*, 2016, **261**, 48–59.
- 18 R. van Hardeveld and F. Hartog, *Surf. Sci.*, 1969, **15**, 189–230.
- 19 A. C. Kizilkaya, J. W. Niemantsverdriet and C. J. Weststrate, *J. Phys. Chem. C*, 2016, **120**, 3834–3845.
- 20 C. J. Weststrate, A. C. Kizilkaya, E. T. R. Rossen, M. W. G. M. Verhoeven, I. M. Ciobică, A. M. Saib and J. W. Niemantsverdriet, *J. Phys. Chem. C*, 2012, **116**, 11575–11583.
- 21 K. M. E. Habermehl-Cwirzen, K. Kauraala and J. Lahtinen, *Phys. Scr., T*, 2004, **108**, 28–32.
- 22 M. M. M. Jansen, J. M. Gracia, A. C. Kizilkaya, B. E. Nieuwenhuys and J. W. Niemantsverdriet, *J. Phys. Chem. C*, 2010, **114**, 17127–17135.
- 23 G. Kresse and J. Hafner, *Phys. Rev. B: Condens. Matter Mater. Phys.*, 1993, **47**, 558–561.
- 24 G. Kresse and J. Furthmuller, *Phys. Rev. B: Condens. Matter Mater. Phys.*, 1996, **54**, 11169–11186.
- 25 J. P. Perdew and Y. Wang, *Phys. Rev. B: Condens. Matter Mater. Phys.*, 1992, **45**, 13244–13249.
- 26 D. Vanderbilt, *Phys. Rev. B: Condens. Matter Mater. Phys.*, 1990, **41**, 7892–7895.
- 27 G. Kresse and J. Hafner, *J. Phys.: Condens. Matter*, 1994, **6**, 8245.
- 28 P. van Helden and I. M. Ciobica, *ChemPhysChem*, 2011, **12**, 2925–2928.
- 29 P. van Helden, J. A. van den Berg and C. J. Weststrate, *ACS Catal.*, 2012, **2**, 1097–1107.
- 30 M. Rosa, S. Corni and R. Di Felice, *Phys. Rev. B: Condens. Matter Mater. Phys.*, 2014, **90**, 125448.
- 31 H. J. Monkhorst and J. D. Pack, *Phys. Rev. B: Solid State*, 1976, **13**, 5188–5192.
- 32 M. Methfessel and A. T. Paxton, *Phys. Rev. B: Condens. Matter Mater. Phys.*, 1989, **40**, 3616–3621.
- 33 A. Ulitsky and R. Elber, *J. Chem. Phys.*, 1990, **92**, 1510–1511.
- 34 I. M. Ciobica and R. A. van Santen, *J. Phys. Chem. B*, 2003, **107**, 3808–3812.
- 35 S. Shetty and R. A. van Santen, *Catal. Today*, 2011, **171**, 168–173.
- 36 C. Benndorf and T. E. Madey, *Surf. Sci.*, 1983, **135**, 164–183.
- 37 M. J. Loeffler and R. A. Baragiola, *J. Chem. Phys.*, 2010, **133**, 214506.
- 38 G. B. Fisher, *Chem. Phys. Lett.*, 1981, **79**, 452–458.